Atomistic simulation of interaction of collision cascade with different types of grain boundaries in α-Fe

A. Kedharnath, Rajeev Kapoor*, Apu Sarkar

Mechanical Metallurgy Division, Bhabha Atomic Research Centre, Mumbai, 400 085, India

A B S T R A C T

Presented here are atomistic simulations of the interaction of a collision cascade in α-Fe with different types of grain boundaries (GBs). The collision cascade was generated by a primary knock-on Fe atom of 3 keV kinetic energy. Four different types of symmetric tilt GB configurations (low angle and high angle GBs, $\Sigma3$ and $\Sigma11$ GBs) with two tilt axes $[1\,1\,\overline{2}]$ and $[\overline{1}\,1\,0]$ were considered. Difference in potential energy, strength and average displacement of atoms between pristine and irradiated GB configurations were analysed to bring out the effect of irradiation. The vacancy and interstitial formation energies calculated using molecular statics simulations were found to be lower in the GB than in the grain. Collision cascade resulted in defect clusters in and around the GB. Low angle GBs were found to be better sinks for radiation induced defects. Tensile deformation of the irradiated configurations resulted in dislocation loops being nucleated from interstitial clusters. The loss in strength after irradiation was high for $\Sigma3$ GBs and negligible for other GBs. It was suggested that materials with low angle GBs and a high dislocation density would be preferred for use in radiation environment.

© 2019 Elsevier B.V. All rights reserved.

1. Introduction

Steels are the primary choice of structural materials in most of the nuclear reactors owing to their superior strength and corrosion resistance and relatively lower cost than other equivalent materials. Austenitic stainless steels are used as cladding material in fast breeder reactors (FBR), low alloy bainitic steels are used as reactor pressure vessel (RPV) material in pressurised water reactor (PWR), ferritic-martensitic (FM) steel is used in FBR for wrapper application, reduced activation ferritic/martensitic steel (RAFM) is recognized as a potential blanket material in fusion reactors [1—5].

As components in nuclear reactors undergo radiation damage it is essential that their mechanical properties under irradiation be well studied. High energy particles interact with the material by transferring their kinetic energy to atoms on collision, creating primary knock-on atoms (PKA). A PKA in turn creates a collision with its neighbouring atoms by transferring its kinetic energy. This process continues resulting in a cascade of collisions. In this process, the pairs of interstitials and vacancies (Frenkel pairs) produced rearrange with time to form clusters and dislocation loops.

To simulate such an event using molecular dynamics (MD) technique, a single atom is given a velocity (kinetic energy) making it a PKA. The displacement of atoms and number of Frenkel pairs increases in few femtoseconds. As the system gradually cools down in a few picoseconds, the kinetic energy of the system, the number of Frenkel pairs and the total displacement of atoms reduce. Many such collision cascades generate defect clusters and dislocation loops. When a PKA is directed perpendicular to a GB plane, the spatial distribution of Frenkel pairs and clusters formed due to the collision cascade in and around the grain boundary would be different from that formed in the grain interior. The spatial configuration and distribution of vacancies, interstitials and defect clusters formed in and around GB influence the way GB behave when mechanically loaded. Thus, the strength of the material before and after irradiation would be different. Results of single collision cascade from MD simulations can be used as inputs to kinetic Monte Carlo (KMC) simulations. In turn the results from KMC can be used as input to higher scale simulation techniques like dislocation dynamics (DD), crystal plasticity (CP) and finite element analysis (FEA) to study and determine the hardening, creep, and fatigue behavior of the nuclear materials in a radiation environment. Results like defect formation energies and sink strength of the GBs could be carried to multiscale modelling techniques [6—9]. Multiscale simulation is an important tool to investigate the

evolution of radiation defects in materials — their generation and annihilation, and MD simulations are an important part of multiscale modelling.

Experimental studies have shown the importance of GBs and dislocations as sinks for point defects, defect clustering and alloying elements segregation [10—14]. Segregation of alloying elements were seen more on dislocation lines than on loops [15—17]. In Fe—Cr alloys, Cr clustered around dislocation loops while defects were absorbed by glissile dislocations [18,19]. The radiation induced segregation of Cr, Ni and Si at prior austenitic grain boundaries [20—22] were seen to influence swelling resistance [23]. The benefits of radiation damage prevention in ultrafine grained materials were demonstrated in ultrafine grained 316SS irradiated with Fe ion beam [24,25].

While the role of GBs during irradiation has been studied experimentally, their interaction with point defects and cluster at the atomistic scale is not well established [26]. MD has the capability to model both the process of collision cascade and the interaction of radiation induced defects with GBs. Guinan and Kinney were the first to publish a work on MD simulation of displacement cascade in tungsten [27]. Following this, there were irradiation simulation works on other bcc metals with different PKA energies. It was shown that when the distance between the initial PKA and GB was small, vacancy clusters were larger and interstitial clusters smaller [28,29]. There were works on irradiation simulations in iron to study the cascade evolution, cluster properties [30—34] and their effects on dislocation lines and loops [35] and GBs [36—38]. Bacon and Rubia simulated cascade evolution in α-Fe and showed that MD is a powerful tool to study radiation damage [39]. Javier Pérez-Pérez and Roger Smith initiated collision cascade in symmetric tilt and twist GBs in bcc iron and concluded that GBs acted as regions for accumulation of damage. They found that damage in the GBs was higher than in the bulk, but they were unable to quantify the effect due to insufficient data [40,41]. Recent articles on radiation damage also emphasise on the importance of grain boundaries and their mechanical properties in radiation environment [42—50]. The above mentioned experimental and simulation results suggest that GBs and dislocations play an important role in irradiation resistance of the material. However, the effect of different types of GBs on irradiation damage has not been sufficiently explored.

The aim of the present work was to use molecular dynamics to simulate and study in α-Fe the effect of collision cascade on different types of symmetric tilt GBs with [1 1 $\overline{2}$] and [$\overline{1}$ 1 0] as tilt axis. Under each tilt axis, four different types of GBs were selected — low angle grain boundary (LAGB), high angle grain boundary (HAGB), Σ 3 and Σ 11 GBs. The evolution of defects, their character and their interaction with different GBs are discussed. The mechanical behavior of configurations with these GBs with and without irradiation induced defects was compared.

2. Simulation methodology

Both molecular statics (MS) and MD simulations were carried out in Large-scale Atomic Molecular Massively Parallel Simulator (LAMMPS) [51]. Mendelev et al. had developed an embedded atom model (EAM) potential which could properly predict the Fe—Fe interaction in radiation damage studies [52]. Since potential stiffening had already been carried for the potential, this potential was directly used in the present work. Point defects, their clusters and their impact on the GBs/dislocations were visualized using Open Visualisation Tool (OVITO) [53]. Periodic boundary conditions (PBC) were applied along all directions during tensile simulation.

2.1. Simulation model

To study the interaction of a collision cascade with different GBs in α-Fe, four types of symmetric tilt GBs were chosen — LAGB, HAGB, Σ 3 and Σ 11 with two tilt axes [1 1 $\overline{2}$] and [$\overline{1}$ 1 0]. The [1 1 $\overline{2}$] tilt axis was selected because this resulted in glissile dislocations in the LAGB on {110} <111> slip system. The [$\overline{1}$ 1 0] tilt axis was selected as this produces a coherent Σ 3 twin boundary. The GB configurations and their crystallographic orientations have been described in an earlier work [54]. The LAGBs and HAGBs are defined using their tilt angle — GBs with tilt angle less than 15° are referred as LAGBs and greater than 15° are referred as HAGBs. The LAGB in the [1 1 $\overline{2}$] tilt axis configuration consisted of glissile dislocations with line direction of [1 1 $\overline{2}$] and Burgers vector of [1 1 1], while the LAGB in the [$\overline{1}$ 1 0] tilt axis configuration consisted of sessile dislocations. The chosen Σ 3 GBs were of incoherent type for the [1 1 $\overline{2}$] tilt axis configuration and of coherent type for the [$\overline{1}$ 1 0] tilt axis configuration. HAGBs were chosen because of their noncoincidence site lattice (CSL) character and high tilt angle characteristics. Σ 11 GBs were chosen because of their CSL and high tilt angle characteristics. The GB model used in the present work is shown in Fig. 1a. The configuration consisted of three crystals C-1, C-2 and C-3 separated by two boundaries, with orientations of C-1 being equal to that of C-3. The GB's atomic configurations were created in LAMMPS by MS technique using conjugate gradient (CG) method. GBs were created in LAMMPS by inputting the three mutual perpendicular lattice directions of the grains. To avoid interaction of cascade and sub-cascade with their periodic images and to ensure that the defects were retained within the simulation box, a box size of 300 Å × 300 Å × 140 Å with nearly 2 million atoms was chosen. GBs were equilibrated using CG method (MS technique) to reach overall lowest energy configuration. The grain boundary energy (GBE or γ_{gb}) was calculated by Ref. [54].

$$\gamma_{gb} = \frac{E_t - n * E_c}{A_{gb}} \tag{1}$$

where E_t is the total (potential) energy of the system, E_c is the cohesive energy of an atom, A_{gb} is the area of the grain boundary and n is the number of atoms. The GBs used in this study and their properties are listed in Table 1.
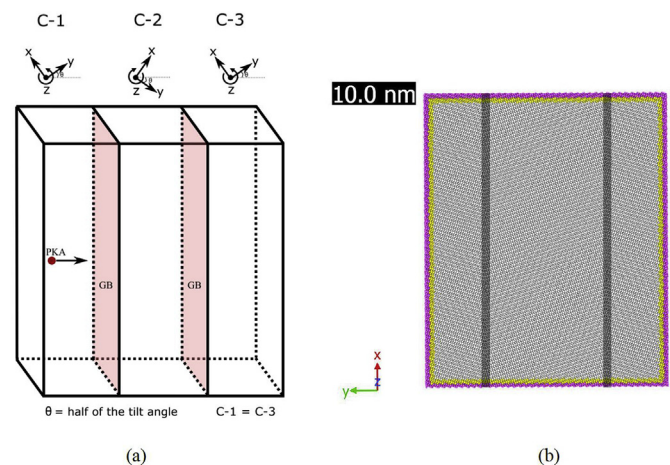

Fig. 1. (a) Schematic representation of grain boundary model used in the current study. (b) Cross section of model showing different layers of atoms for collision cascade simulations. The pink, yellow and grey atoms represent fixed atoms, heat sink atoms and mobile atoms respectively. The grey strip represents grain boundary region. (For interpretation of the references to color in this figure legend, the reader is referred to the Web version of this article.)

Table 1
Properties and values related to different GBs, direction of primary knock on atom, loading direction, the corresponding slip system with the highest Schmid factor and the value of the Schmid factor.

GB related					Collision cascade related	Tensile simulation related			
Tilt axis	GB type	Tilt angle (°)	GB plane	GBE (mJ/m²)	PKA direction	Loading direction	Slip plane	Slip direction	Schmid factor
[1 1 $\bar{2}$]	LAGB	4.9	(20 18 19)	558	[18 20 19]	[$\bar{5}$9 55 $\bar{2}$]	($\bar{1}$ 1 $\bar{2}$)	[$\bar{1}$ 1 1]	0.479
	HAGB	32.5	(19 9 14)	1405	[9 19 14]	[$\bar{2}$6 16 $\bar{5}$]	($\bar{2}$ 1 $\bar{3}$)	[$\bar{1}$ 1 1]	0.495
	Σ 3	180	(1 $\bar{1}$ 0)	374	[$\bar{1}$ 1 0]	[$\bar{1}$ $\bar{1}$ $\bar{1}$]	(2 1 1)	[$\bar{1}$ 1 1]	0.314
	Σ 11	62.96	(7 1 4)	646	[1 7 4]	[$\bar{3}$ 1 $\bar{1}$]	(1 $\bar{1}$ 0)	[1 1 1]	0.445
[$\bar{1}$ 1 0]	LAGB	4.91	($\bar{1}\bar{1}$33)	643	[1 1 33]	[$\bar{3}$3 $\bar{3}$3 2]	(1 1 $\bar{2}$)	[1 1 1]	0.484
	HAGB	31.6	($\bar{1}$ $\bar{1}$ 5)	1470	[1 1 5]	[$\bar{5}$ $\bar{5}$ 2]	(1 1 $\bar{2}$)	[1 1 1]	0.489
	Σ 3	70.5	($\bar{1}$ $\bar{1}$ 2)	291	[1 1 2]	[$\bar{1}$ $\bar{1}$ 1]	(1 1 $\bar{2}$)	[1 1 1]	0.314
	Σ 11	129.5	($\bar{3}$ $\bar{3}$ 2)	1208	[3 3 2]	[$\bar{1}$ $\bar{1}$ 3]	(0 $\bar{1}$ 1)	[$\bar{1}$ 1 1]	0.445

2.2. Defect formation energy

Vacancy and interstitial formation energies (VFE and IFE respectively) were calculated in and around GB for different GB configurations using MS technique. A vacancy was created by deleting an atom, and an interstitial was created by adding an extra atom. The system was equilibrated using CG method and the energy of the system was calculated. The vacancy/interstitial formation energy (*VFE/IFE*) was calculated as the difference in energy between the initial configuration and the configuration with vacancy/interstitial [55,56], i.e.

$$VFE = E_v - (E_t - E_c) \qquad (2)$$

$$IFE = E_i - (E_t + E_c) \qquad (3)$$

where E_v and E_i are energies of the configuration with a vacancy and an interstitial respectively, E_t is the total energy of the pristine GB configuration and E_c is the cohesive energy of an atom. A series of simulations with vacancy/interstitial created at different location from GB were carried out to determine the defect formation energy (DFE) as a function of distance from the GB. Total of 80 simulations for each GB configurations were carried out by either adding an atom (to create interstitial) or deleting an atom (to create vacancy). These simulations were carried out starting from 20 Å from one side of the GB to 20 Å on the other side with a step size of 0.5 Å. The ability of the GB to act as a sink for defects was quantified using a parameter called the sink strength and was calculated as [56].

$$Sink\ Strength = \frac{\left(DFE_{grain} - DFE_{gb}\right)}{DFE_{grain}} \qquad (4)$$

DFE_{grain} and DFE_{gb} were the defect formation energies in the grain and grain boundary respectively. Here *DFE* represents either *VFE* or *IFE* as given by eqs. (2) and (3) respectively.

2.3. Collision cascade simulation

To prepare the GB configurations for collision cascade simulations, the outermost layer of the simulation box with 5 Å thickness was fixed throughout the collision cascade simulation. The next layer with 10 Å thickness was equilibrated using Nose-Hoover thermostat (NVT ensemble) at 0 K throughout collision cascade simulation to act as heat sink. The remaining innermost atoms were allowed to evolve dynamically using microcanonical (NVE) ensemble. The cross-section view of the model with different layers of atoms is shown in Fig. 1 (b). An atom at a distance of 30 Å from the GB was imparted a velocity equivalent to 3 keV kinetic energy perpendicular to the GB plane; this atom is called PKA. The damage

energy and PKA distance from the GB were selected such that the cascade interacted with the GB and was also contained within the simulation box. The cascade simulation was run initially for 0.8 ps with 0.001 fs time-step, then with 0.01 fs time-step till 13 ps and finally with 0.1 fs time-step till 150 ps. In the later part of the computation as there were little changes in Frenkel pair generation the time-step was increased to 0.1 fs. The simulations were run at 0 K to minimize the thermal effects so as to study only the effect of cascade on GB structures. To incorporate statistical variations in the simulations, for each grain boundary configuration six cascade simulations were carried out. This was done by varying the direction of PKA by angle of 2° from the normal to the grain boundary (i.e. simulation done for PKA at angle of 2°, 0° and −2° to the boundary normal) and temperature of system varied by 5 K (i.e. simulation done for 0 and 5 K). The evolution of collision cascade for each GB configuration was studied using average displacement of atoms and number of Frenkel pairs. Difference in potential energy between pristine (unirradiated) GB configurations and irradiated GB configurations gave the extra energy stored because of radiation induced defects. During cascade simulation, the average displacement of atoms and number of Frenkel pairs were recorded. The average displacement of n atoms was calculated using $\frac{\sum_{i=1}^{n}\sqrt{(dx_i^2+dy_i^2+dz_i^2)}}{n}$, where dx_i, dy_i and dz_i were the change in the atomic positions at any instant of time with respect to the initial time. Frenkel pairs were found using Voronoi tessellation in LAMMPS [57]. Voronoi cells were constructed before the start of the simulation and the number of atoms in each Voronoi cell was counted at every timestep. A count = 0 in a Voronoi cell represented the presence of a vacancy. Count >1 represented interstitial(s) while count = 1 represented pristine lattice atom. Generation of an interstitial correspondingly produces a vacancy, this pair is called as Frenkel pair. If more than one point defect of the same type (either vacancy or interstitial) were located together it was considered as a defect cluster. This visualization of Frenkel pairs helped in understanding the production and recombination of point defects and formation of defects clusters. To quantify GBs as regions of defect sinks, potential energy and hydrostatic stress on the atoms in and around the GB region were mapped. Hydrostatic stress on the atoms is $\frac{1}{3}(S_x + S_y + S_z)$ where S_x, S_y and S_z are the normal stresses on the atoms along x, y and z directions respectively. After cascade simulation, point defects and defect clusters distributions were visualized in OVITO using CNA & potential energy, Frenkel pairs counts and dislocation extraction algorithm (DXA) [53,58,59]. After CNA was carried out, atoms with bcc lattice structure were deleted and the remaining atoms were colored using potential energy values. DXA followed by the deletion of atoms was carried out to visualize and analyse the damage in the dislocations due to radiation induced defects.

2.4. Tensile simulation

The mechanical behavior of the configurations with GBs/dislocations in the presence of radiation induced defects and effect of spatial configuration of these defects during tensile loading was studied. Tensile simulations were carried out on each of the six sets of collision cascades for each GB configuration. The irradiated GB configurations were pulled uniaxially perpendicular to the GB normal at a constant strain rate of $10^{10}\,\text{s}^{-1}$ till a strain of 0.35 (lasted for 35 ps). During the deformation, the temperature was maintained at 0 K to minimize the thermal effects and the strain along other two directions were made zero using isobaric-isothermal (NPT) ensemble. The stress and strain values along the loading direction were stored at every timestep. Similar set of tensile simulations were carried out in pristine GB configurations.

From the simulations the potential energy, average displacement of atoms, number of Frenkel pairs at the end of the cascade simulation and the ultimate tensile strength were determined for each GB configuration. This comparative study on different GB configurations brought about an understanding of their ability to act as sinks for defects. The simulation methodology is summarised in Fig. 2. Initially the GBs were equilibrated and DFE was calculated using MS technique. Subsequently MD was used to produce a cascade of defects using a primary knock-on atom. Finally, tensile simulations were carried out on both the irradiated and pristine configurations of different GB configurations.

3. Results

The properties of the selected GBs with two different tilt axes are tabulated in Table 1. The table also lists the PKA direction and details of the loading geometry. The GBE, tilt angle and GB plane of different GBs are tabulated under GB properties. The PKA direction is along GB normal and as the GB configurations for each case are different, the crystallographic directions of the PKA in each GB configurations are also different. The results of collision cascade analysis, defect analysis and tensile analysis with respect to the GBE and atomic structure of both the pristine and the irradiated GB are presented here for the simulations carried out at 0 K and with PKA at 0° to the GB plane normal. The results using other conditions (−2° and 2° deviation from GB plane normal and at 5 K) were used to determine the scatter and are shown as error bars in appropriate graphs.
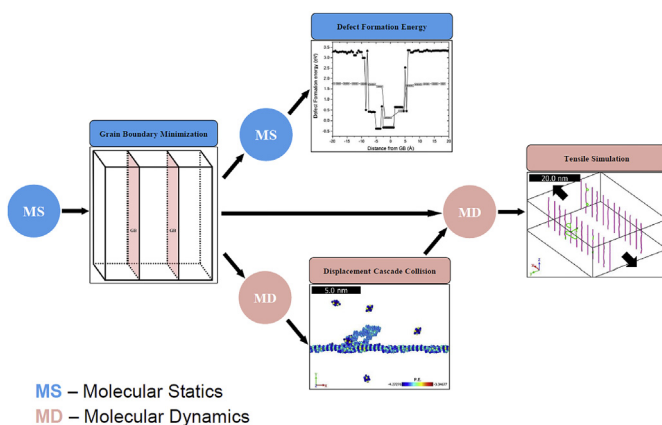

Fig. 2. Work flow of the current study of collision cascade simulation. Arrows in the tensile simulation indicate direction of loading. MS — Molecular Statics; MD — Molecular Dynamics.

3.1. Defect formation energy

The defect formation energies for both tilt axis configurations are shown in the Fig. 3. Vacancy (interstitial) formation energy in the grain was nearly same for all GB configurations and therefore the average displacement and the number of Frenkel pairs in the grain region for different GB configurations was also same. In all cases, it was seen that the defect formation energies were relatively lower in the GB region than in the grain. This could be because of the spatial atomic arrangement in the GB giving extra space for the accommodation of defects. The lower defect formation energy at GBs would also favour the trapping of these defects at GBs. A positive DFE signifies an endothermic process and a negative one an exothermic process [56]. All GB configurations had positive DFE, except LAGB with $[\bar{1}\,1\,0]$ tilt axis which showed a negative IFE. LAGB consists of sessile dislocations of type $\langle 1\,0\,0 \rangle$ and a dislocation line direction of $[\bar{1}\,1\,0]$. The Σ 3 configurations showed similar DFE values in the grain and GB region because the volume of the unit cell in the GB was almost equal to the volume of the unit cell in the grain. This is expected as defects disturb the coherency of the Σ 3 GBs, and thus are unlikely to hold defects in the GB region.

3.2. Collision cascade analysis

Fig. 4 shows the average displacements of atoms and number of Frenkel pairs produced as a function of time during collision cascade simulations in α-Fe with different GBs (one out of six sets). The statistical variations in average displacements of atoms and number of Frenkel pairs of six set of each GB configurations will be discussed later. During cascade interaction with the GB, the GB structure broke because of displacement of the atoms from their position in the GB region. When the system cooled down, due to the absorption of defects in the GB region, broken GB structure self-healed itself forming a bulge in the GB region. Alternately it can be said that the GB had migrated out of its plane. Finally, stable point defects and defect clusters were formed in and around GB. The supplementary videos V1-V3 show the interaction of collision cascades with GB. In the videos, kinetic energy is mapped on non-bcc atoms after CNA analysis. Although PKA travelled through differently oriented grains in different GB configurations (anisotropy), because of the high velocity of the PKA, the initial average displacement of the atoms and number of Frenkel pairs increased with time and were nearly same for all GB configurations till 0.07 ps (Fig. 4). The average displacement of atoms continued to increase non-linearly during the interaction of the cascade with the GB and reduced during the cooling period. The number of Frenkel pairs over time was controlled by three factors − generation due to collision cascade, recombination of defects and absorption of defects in the GB. The high displacement of atoms at the start of the interaction of cascade with the GB resulted in the number of Frenkel pairs increasing. Later, due to defect absorption there were fluctuations in the number of Frenkel pairs till 0.8 ps. Finally the recombination and absorption of defects in the GB regions decreased the number of Frenkel pairs in the system.

Supplementary video related to this article can be found at https://doi.org/10.1016/j.jnucmat.2019.06.021

The ability of the GB to prevent the cascade from penetrating it was different for different GBs depending on their GBE and GB atomic structure. As Σ 3 GBs had thin and narrow GB regions (due to the higher coincidence of lattice sites), the cascade could penetrate the GB and form defects on the other side of the GB. Visualization of defects after the system had cooled at the end of the simulation is shown in Fig. 5. Other GBs showed little penetration of cascade into the GB region (see Fig. 5 (II)). The average displacement of atoms and number of Frenkel pairs were different
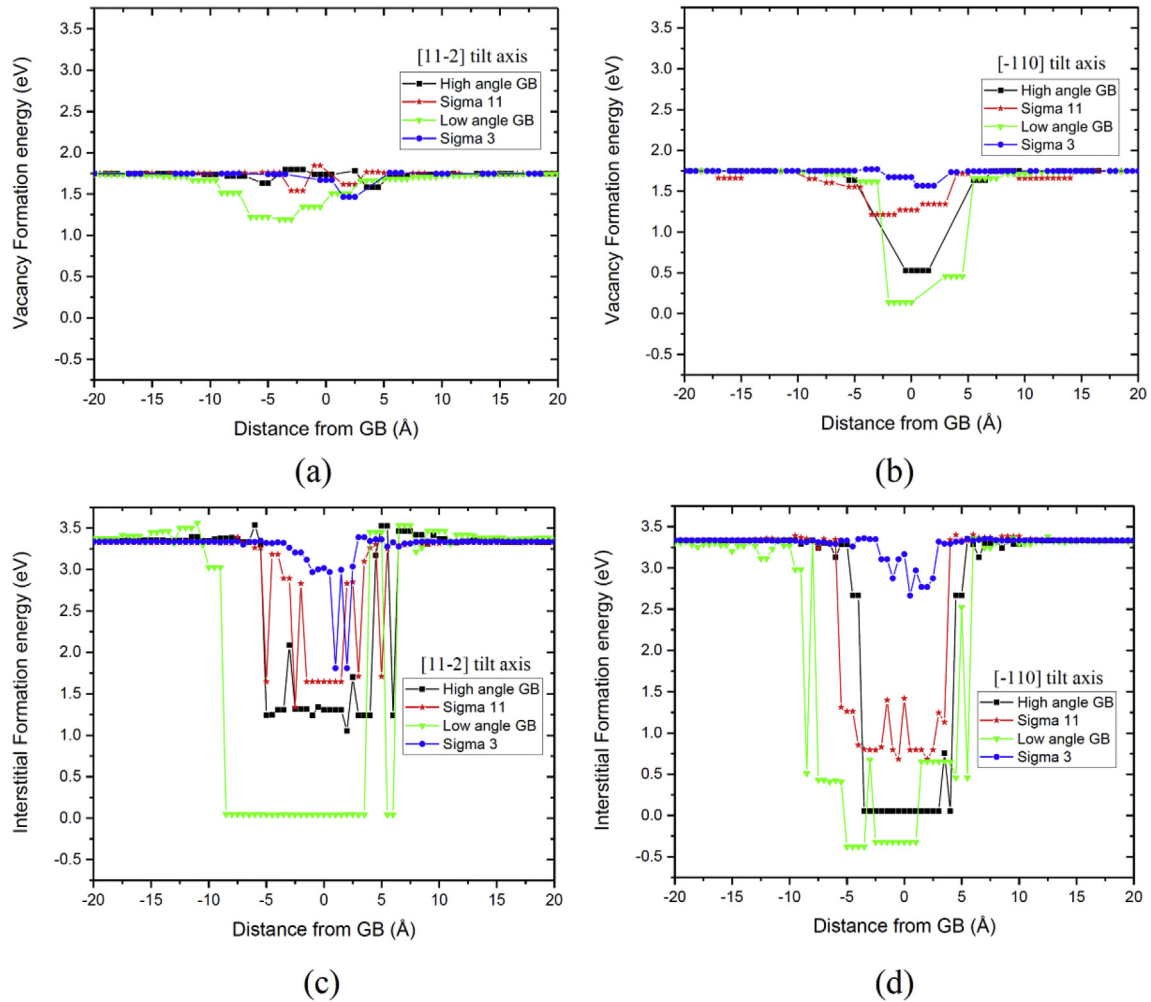
Fig. 3. Defect formation energies of vacancies and interstitials in $[11\bar{2}]$ tilt axis GBs (a, c), and in $[\bar{1}10]$ tilt axis GBs (b, d).

for different GBs because of the differently oriented grains in reference to the direction of the PKA, their GBE, the GB structure (which acted as barrier for the cascade and sink for the defects) and the defect formation energy in the GB region. The direction of PKA for different GB configurations is listed in Table 1.

It was observed that there was a biased absorption of vacancies as compared to interstitials in the GBs. For most configurations, the absorption of interstitials in the GB was preferred over that of vacancies, except for the Σ 3 GB configuration (Fig. 3). This can be attributed to the lower value of IFE as compared to VFE in the GB. As stress in the lattice due to an interstitial is compressive, it is likely that the interstitials get absorbed in the tension part of the GB region. Similarly, it is likely that vacancies (which produce tensile stress in lattice) get absorbed in the compression part of the GB region. Some interstitials and vacancies recombine in the GBs, while the excess vacancies and interstitials remain trapped in the GB region due to insufficient kinetic energy.

Fig. 5 (I) shows the mapping of hydrostatic stress on the atoms in pristine GB configuration. It is seen that a combination of tension and compression fields exist in the LAGB due to the presence of individual dislocations. Top view of the Σ 3 and Σ 11 GBs showed that the GB experiences compression on one side and tension on the other. LAGBs and Σ GBs had defined regions having positive and negative hydrostatic stress fields and were therefore potential sites for sinks of vacancies and interstitials. It is seen that these sessile

dislocations have a high hydrostatic stress field (Fig. 5 (a) (I)) and could thus accommodate interstitials, explaining the low observed IFE. HAGB had mixed stress fields and so the sink regions were not identifiable. Fig. 5 (II) shows the final number of Frenkel pairs trapped and their position in and around the GB. GB region was shown with a semi-transparent black colored slab to visualize the defects accumulated in the GB region. The width of the slab was calculated from the width of the non-bcc atoms (after common neighbour analysis (CNA)) in the GB region. Fig. 5 (III) shows the mapping of potential energy on non-bcc atoms after CNA. Non-bcc atoms represented distorted lattice atoms. Deviation of atoms from its lattice position in the GB gave rise to the increase in the energy in the GB. From Fig. 5 (I), (II) and (III) it is seen that in places where vacancies (interstitials) were absorbed in the GB, interstitials (vacancies) too were trapped in the same part of the GB. From Fig. 5 (I) and (II), it was observed that in LAGBs the interstitials were trapped in the tension part and vacancies were trapped in compression part of the dislocation kink. In HAGBs there was a mixed trapping of defects due to no clear demarcation of the tension and compression part of the stress field. These trapped defects in the GB are expected to affect the strength of the GB region. Cumulative effect of GBE, GB structure, sink strength of GBs and stress fields on the GBs affected the average displacement of atoms and number of Frenkel pairs over simulation time. The simulation video of the variation of Frenkel pairs is shown in supplementary video V4.
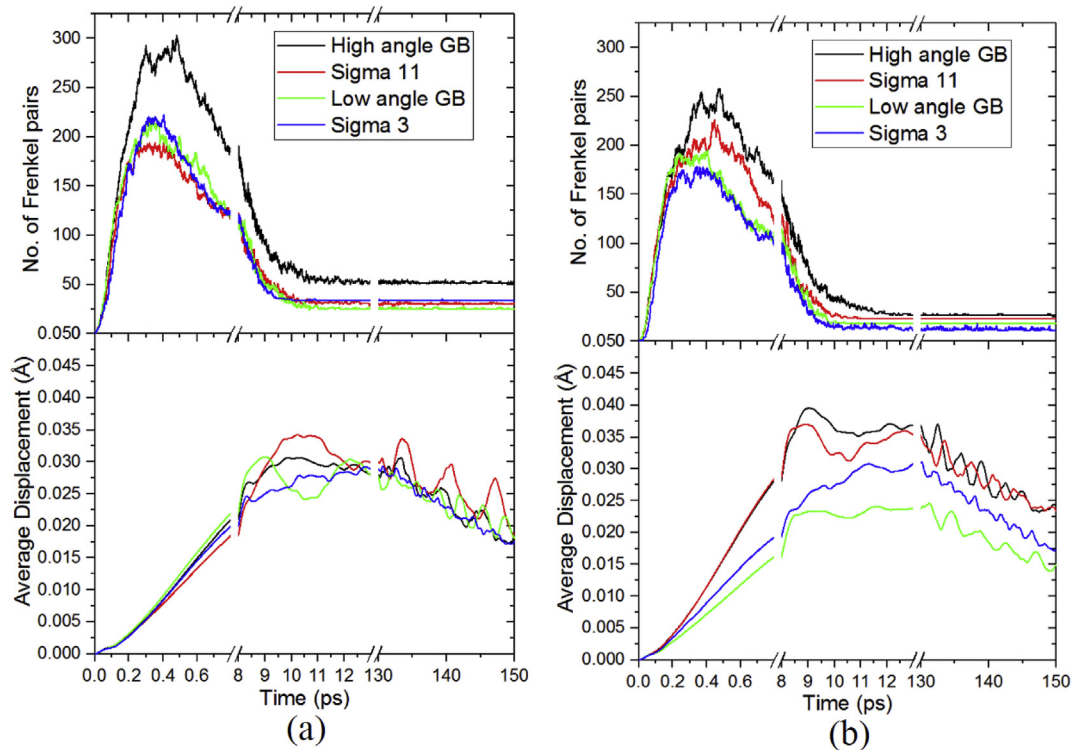
Fig. 4. Number of Frenkel pairs and average displacement of atoms in (a) [11$\bar{2}$] and (b) [$\bar{1}$10] tilt axis GB configurations.

Supplementary video related to this article can be found at https://doi.org/10.1016/j.jnucmat.2019.06.021

3.3. Defect analysis

The defect cluster configuration and distribution in and around GB were analysed after the system had cooled down to 0 K (shown in Fig. 6). Fig. 6 (a) and (b) shows non-bcc atoms surrounding a vacancy and an interstitial. It is seen that the stress field and non-bcc atoms generated around interstitials are more than that around vacancies. As vacancies generate isotropic hydrostatic stress field around them, they form a more isotropic clustering as compared to interstitials that have an anisotropic stress field around them due to dumbbell formation. Clusters with more than 5 vacancies were seen in all GB configurations. As VFE < IFE within grains, vacancy clusters were preferred in the grain. In most cases (other than Σ 3), as VFE was higher than IFE in the GB more interstitials formed in the GB. Defects were analysed with respect to the defect distribution and their clustering properties using DFE and stress fields in the GB. Both DFE and stress fields played an important role in defect absorption and trapping.

3.3.1. LAGB

Away from the GB, interstitial point defects and small vacancy clusters were seen (Fig. 5 III). Fig. 6 (c) shows the details of such clusters. As LAGBs had lower VFE in the GB as compared to the grain, more vacancies formed in the GB than in the grain. Also, fewer vacancy clusters were seen in the grain of the LAGB configurations as compared to other GB configurations. In the LAGB configuration with [1 1 $\bar{2}$] tilt axis, initial line length of the central dislocations was 168 Å, which after cascade interaction increased to 171 Å (Fig. 6 d). In LAGB with [$\bar{1}$ 1 0] tilt axis, the dislocation line length increased from 137 Å to 147 Å (Fig. 6 l). The increase in dislocation line length was due to the formation of kinks on the dislocation line. Kinks forms

because during collision cascade, the dislocation line breaks, and on cooling the defects recombine and get absorbed in the dislocation to form kinks of screw type. This self-healing property of LAGBs was observed to be better than that of other GBs.

3.3.2. HAGB

HAGB consisted of ⟨1 1 1⟩ and ⟨1 0 0⟩ types of dislocations. After cascade interaction, the HAGB generated ⟨1 1 0⟩ partial dislocation along with ⟨1 1 1⟩ and ⟨1 0 0⟩ types of dislocations forming a network of dislocations as seen in Fig. 6 (g). This generation of partial dislocations ensured that the HAGB remained intact and hence it can be said that HAGBs have a property of self-healing. Further, as the hydrostatic stress field distribution at the GB is of mixed character, the distribution of vacancies and interstitials too are random. In HAGB with [1 1 $\bar{2}$] tilt axis, VFE in GB was almost equal to that in the grain which facilitated vacancies to form vacancy loops near the GB as in Fig. 6 (e, f). When viewed along [1 1 $\bar{2}$] direction, vacancy loop had an elliptical shape (Fig. 5 a II). In addition to these observations, an interstitial cluster away from the GB (Fig. 6 m) and semi-vacancy loop near GB (Fig. 6 n) were seen.

3.3.3. Σ 3 GB

Σ 3 GBs had the largest number of interstitial clusters as compared to other GB configurations. The interstitial clusters contained about 2–5 interstitials as shown in Fig. 6 (h, i, o, p, q). In [1 1 $\bar{2}$] tilt axis configuration, the Σ 3 GB was incoherent having compressive and tensile stress fields on either side of the GB. Vacancies clustered (trapped) more in the GB than in the grain and few interstitial point defects were seen in GB. In [$\bar{1}$ 1 0] tilt axis configuration, the Σ 3 GB was coherent with a very narrow GB region so DFE in the GB was almost equal to that in the grain. This resulted in less trapping of defects in the GB. When viewed along [$\bar{1}$ 1 0] direction it could be seen that the GB had a tensile field enabling interstitials to get trapped in the GB region. A large

Tilt axis | **GB type** | **Stress (I)** | **Frenkel Pair (II)** | **CNA & P.E. (III)**

[11\overline{2}]

LAGB
HAGB
Σ 3
Σ 11

(a)
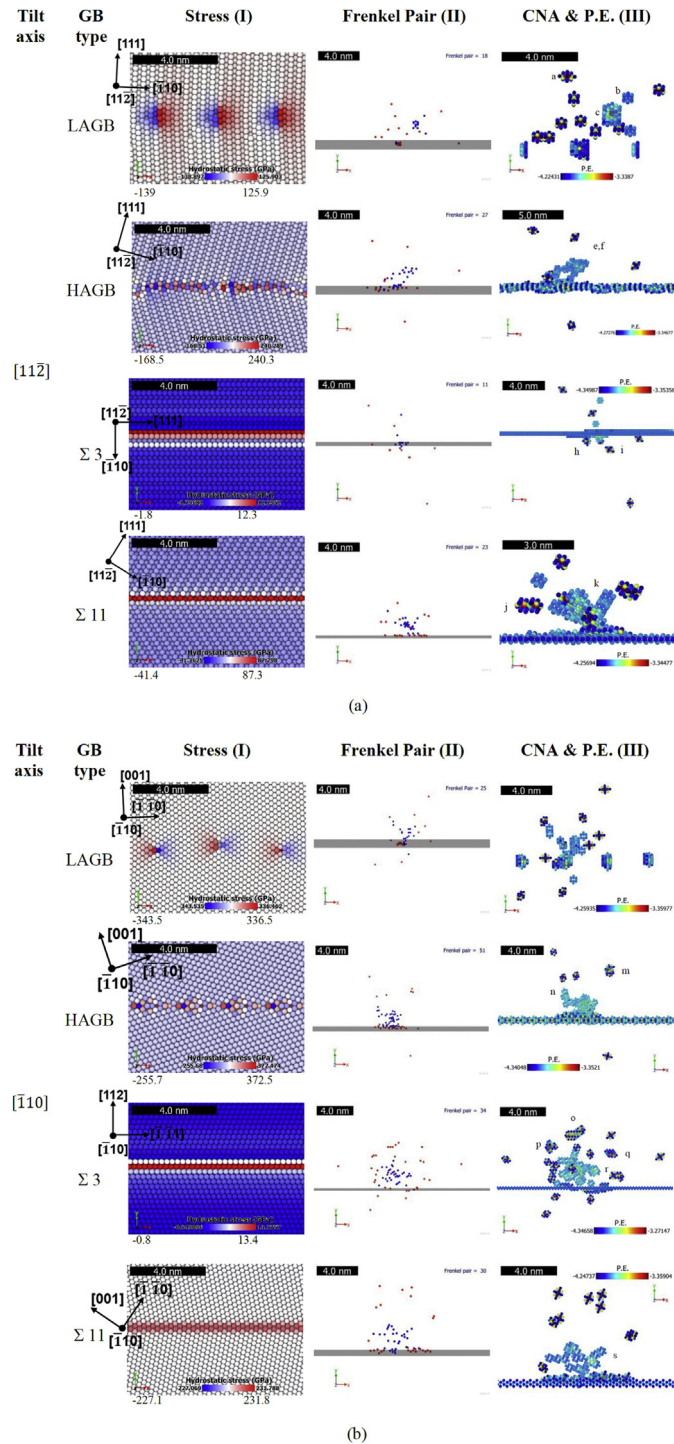
[\overline{1}10]

LAGB
HAGB
Σ 3
Σ 11

(b)

Fig. 5. Stress mapping of atoms in pristine GB configurations (column I), Frenkel pair (column II) and CNA & potential energy (P.E.) (column III) mapping in irradiated GB configurations of (a) [11$\overline{2}$] tilt axis GBs and (b) [$\overline{1}$10] tilt axis GBs. In column I, the directions help in understanding the rotation of the crystal. In column II, blue colored atoms represent vacancies and red colored atoms represent interstitials. GB region was shown with a semi-transparent black colored slab. In column III, each defect is named in alphabetical order and is shown individually in Fig. 6. (For interpretation of the references to color in this figure legend, the reader is referred to the Web version of this article.)

vacancy cluster sticking to an interstitial cluster (Fig. 6 r) and 3 independent interstitials clusters were seen inside a grain, with 2, 3, 5 interstitials in each of them (Fig. 6 o, p, q).

3.3.4. Σ 11 GB

Σ 11 GBs had irregular vacancy clusters in the grain (Fig. 6 k, s). In Σ 11 with [1 1 $\overline{2}$] tilt axis, IFE was almost equal to VFE within the GB. In Σ 11 with [$\overline{1}$ 1 0] tilt axis, clusters of interstitials and few vacancies were seen in and near the GB. The Σ 11 GBs with [$\overline{1}$ 1 0] tilt axis showed a larger number of defects and clusters in the grain and GBs as compared to that with the [1 1 $\overline{2}$] tilt axis.

3.4. Tensile analysis

Stress strain behavior of both pristine and irradiated GB configurations (one out of six simulation tests) is shown in Fig. 7. The strength of the configuration for both the tilt axis is in the order: Σ 3 > LAGB > HAGB > Σ 11. The difference in UTS values in different pristine GB configuration was most probably due to the difference in the orientation of the grain with respect to the loading axis [54]. The loading direction and slip system with the highest Schmid factor for each configuration is shown in Table 1. Σ 3 GBs showed a large difference in UTS between pristine and irradiated GB configurations, whereas other GB configurations showed no significant loss in UTS after irradiation. During loading, radiation induced defects are expected to act as stress raisers which could result in nucleation of further defects[*].

In configuration with LAGBs, interstitials were seen to act as a nucleating site for dislocation loops (Fig. 8 a). With increasing strain the dislocation loop size increased and point defects were formed around the loop. In LAGB with [1 1 $\overline{2}$] tilt axis, dislocation loops with ⟨1 1 1⟩ type interacted with $\frac{1}{2}$⟨1 1 1⟩ dislocations in the GB giving out more dislocations of type ⟨1 1 1⟩ and few of type ⟨ 1 0 0⟩. In LAGB with [$\overline{1}$ 1 0] tilt axis, the ⟨1 1 1⟩ type dislocation loop nucleated from interstitials which interacted with the dislocation of ⟨1 0 0⟩ type in the GB (Fig. 8 b). This interaction along with the applied strain, nucleated ⟨1 1 1⟩ type of dislocation loops from the GB into the grain.

The application of strain to the HAGB configuration with [1 1 $\overline{2}$] tilt axis resulted in the collapse of the partial dislocations in the GB due to overlap of dislocation cores. Dislocation loops nucleated from the GB as seen in Fig. 8 (c). However, the presence of defects in the irradiated GBs had negligible effect on the strength of the configuration as compared to that of the pristine GB configuration. The application of small strain to HAGB configuration with [$\overline{1}$ 1 0] tilt axis created many partial dislocations. With further strain, partial dislocations combined to give ⟨1 1 1⟩ dislocation loops from the GB. The dislocation loops also formed from the defect clusters in the grain and near GB. At higher strains the dislocation loops from the GB interacted with the defect clusters within the grain (Fig. 8 d). Similar events of dislocation loop nucleation from the GB was also seen in pristine GB configuration.

The high strength of the configuration with Σ 3 GBs was possibly due to the coherency of the GB. In Σ 3 with [1 1 $\overline{2}$] tilt axis configuration, the interstitials aligned along ⟨1 1 0⟩ direction and created a fault in the GB (Fig. 8 e). With applied strain, ⟨1 1 0⟩ interstitial configuration rotated to ⟨1 1 1⟩ extending the fault along the GB plane (Fig. 8 f, g, h). This extended fault in the early stage of tensile loading resulted in loss in the strength of the GB. In Σ 3 with [$\overline{1}$ 1 0] tilt axis, the interstitial aligned along tilt direction in the GB plane. The interstitial configuration rotated towards the loading direction making the GB weak. Simultaneously, the defect cluster nucleated dislocation loops which interacted with the GB. This interaction induced nucleation of dislocations on the other side of the GB.

---

[*] During tensile deformation, the existing defects did not return to their original lattice positions, instead they moved in certain directions or nucleated other defects. Similar observations were reported in the work of Kang et al. [60] and Singh et al. [50].
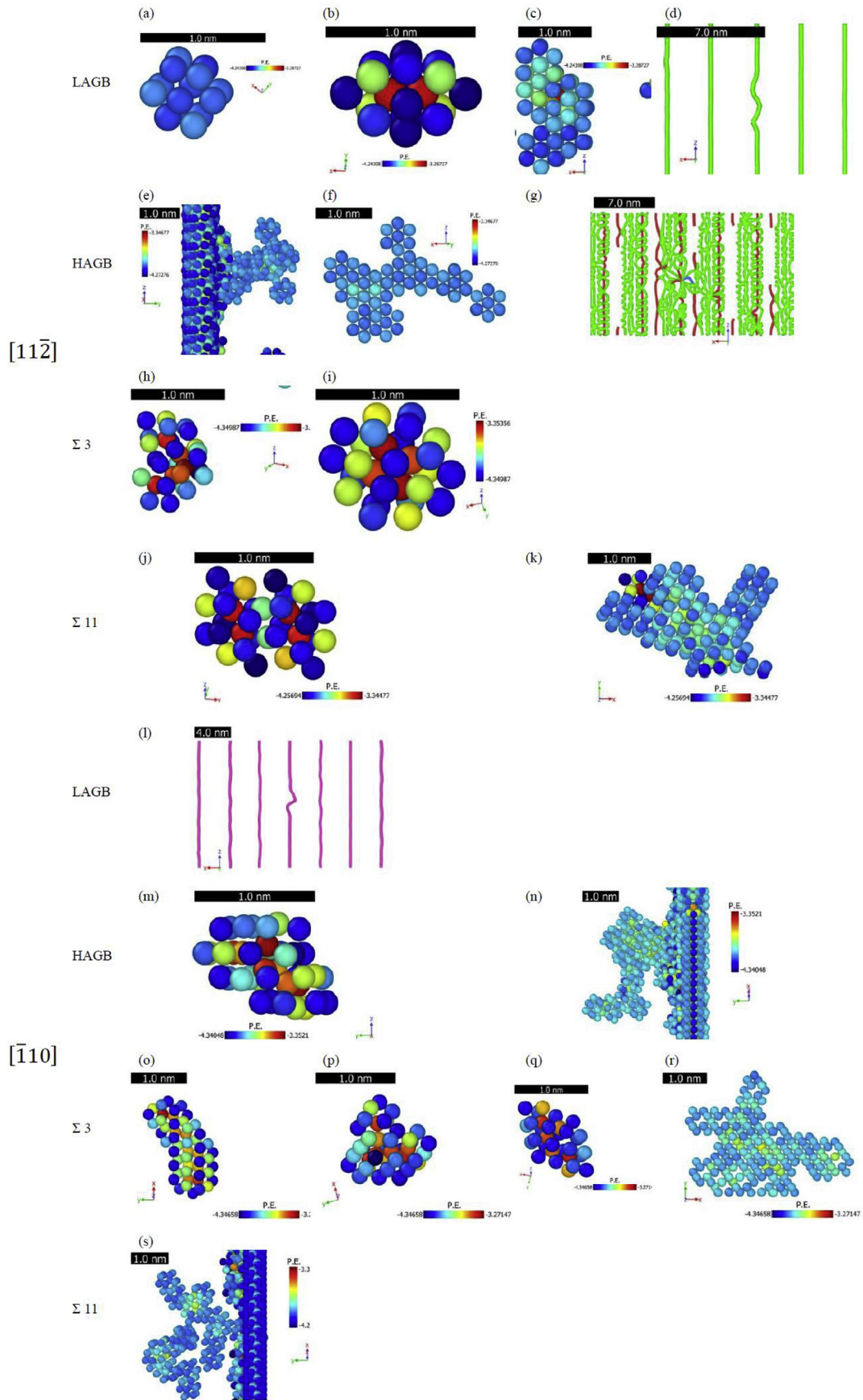
Fig. 6. Examples of defect analyses of different point defects and defect clusters colored by potential energy of non-bcc atoms. Dislocation analysis of LAGB (d, l) and HAGB (g) were carried out using DXA in OVITO. Glissile ($\langle 1\,1\,1\rangle$ type), sessile ($\langle 1\,0\,0\rangle$ type), $\langle 1\,1\,0\rangle$ type and other types of dislocations were colored green, pink, blue and red respectively. The defects named in Fig. 5 (column III) were shown clearly. (a) and (b) represent non-bcc atoms in the presence of vacancy and interstitial respectively. Defect clusters in $[11\bar{2}]$ tilt axis GBs are shown: (c) in LAGB, (e, f) in HAGB, (h, i) in Σ3 and (j, k) in Σ11. Defect clusters in $[\bar{1}10]$ tilt axis GBs are shown: (m, n) in HAGB, (o, p, q, r) in Σ3 and (s) in Σ11. (For interpretation of the references to color in this figure legend, the reader is referred to the Web version of this article.)
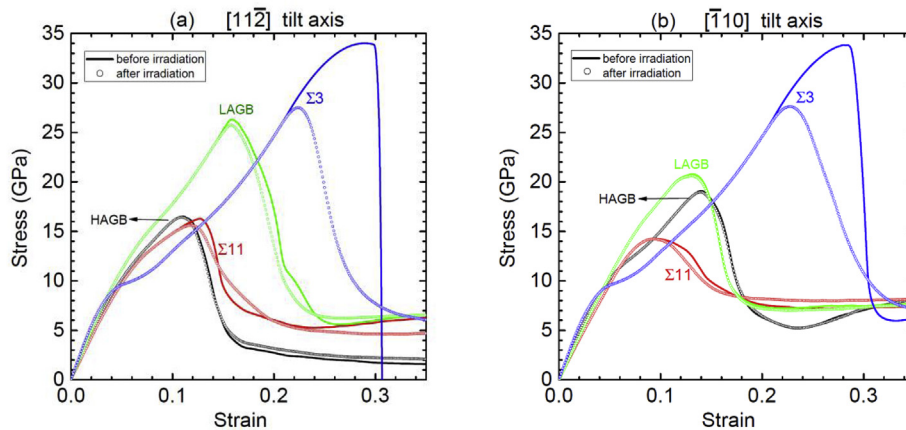
Fig. 7. Stress strain behavior of different configurations having GBs with (a) $[11\overline{2}]$ tilt axis and (b) $[\overline{1}10]$ tilt axis. Solid lines are for unirradiated condition and the symbols are for irradiated condition.

In configuration with Σ 11 GBs, dislocations nucleated from the GB in both pristine and irradiated conditions. In the irradiated condition, the defects near the GB also started nucleating dislocations which resulted in the decrease in the UTS. In Σ 11 with $[1\,1\,\overline{2}]$ tilt axis, the interaction of the collision cascade with the GB created faults in the GB as seen in Fig. 8 (i, j, k, l). Tensile simulation videos of pristine (V5) and irradiated (V6) LAGB configurations are attached in Supplementary section.

Supplementary video related to this article can be found at https://doi.org/10.1016/j.jnucmat.2019.06.021

4. Discussion

Through molecular dynamics simulation of self-ion irradiation in α-Fe the creation of Frenkel pairs, changes in potential energy and strength of the configuration were studied. Each type of grain boundary had different characteristics. HAGBs had mixed stress fields, high GBE and wider GB width. Σ 3 had low GBE and narrow GB width. LAGB had low GBE and periodically distributed dislocations in the GB. These differences of the GB structure affect the annihilation/absorption of vacancies and interstitials in the GB. The sink strength of the GBs and the formation energy of the point defects depended on the GBE and the atomic structure in the GB. Apart from GBs, dislocations also acted as sinks for radiation induced defects. Dislocation type, dislocation density and stress field around dislocations also affect the interaction of defects with dislocations.

The number of Frenkel pairs created during initial cascade interaction depended on the average displacement of atoms, which in turn depended on the grain orientation. The recombination and absorption by the GB affected the final number of Frenkel pairs (i.e. after the cooling of the cascade). After the cascade cooling, defects were seen trapped in and around the GBs. The final number of Frenkel pairs remaining in each configuration is shown in Fig. 9. The HAGB configuration with $[11\overline{2}]$ as tilt axis, showed that a large number of Frenkel pairs remained after collision cascade (higher number of Frenkel pairs as compared to other GB configurations). The LAGB configuration (especially LAGB with $[\overline{1}\,1\,0]$ tilt axis) initially showed the generation of a large number of Frenkel pairs, but after cascade cooling the number of Frenkel pairs reduced. This implies that LAGBs are good absorbers of defects. This result was supported by the high sink strength (eq. (4)) of LAGB for both vacancies and interstitials as seen in Fig. 10.

Sessile dislocations of type <100> in the LAGB had the highest sink strength because of their ability to accommodate defects in their less packed density directions. Dislocations in LAGBs and HAGB not only had good sink strength but also had a good self-

healing property as seen in supplementary videos (V7–V9). Similar observations of such properties were seen in Tschopp's work [55] in which the effect of GBE of different Σ boundaries on site defect density and formation energy of defects were studied. In the present work, the dislocation line damaged during the collision cascade, reconstructed itself by the absorption of defects resulting in the formation of kinks, dislocation loops and dislocation nodes (Fig. 6 d, g, l). These atomistic results help in understanding irradiation resistance through self-healing of materials. Σ 3 GBs for the $[1\,1\,\overline{2}]$ tilt axis had lowest number of Frenkel pairs (Fig. 9) and a low sink strength (Fig. 10), most likely linked to the coherency of the GB structure and the narrow GB width. When compared to other GB configurations, Σ 3 GBs were unlikely to absorb either interstitials or vacancies as these would lead to loss of coherency. An earlier study on the effect of irradiation damage in twist and tilt GBs in α-Fe found that interstitial absorbency at GBs depended on its atomic structure [61]. Interstitial loops though not observed here were seen in Marinica's [62] and Xu's [63] work.

Supplementary video related to this article can be found at https://doi.org/10.1016/j.jnucmat.2019.06.021

In experimental studies, the quantification of defects and the extent of damage have been correlated to the parameter of displacement per atom (dpa). Dpa is calculated using Norgett Robinson Torrens (NRT) formulation in which the damage energy and displacement energy are used [30,64]. However, while calculating dpa using NRT formulation, the sink effect due to GBs and dislocations have not been considered, thus making the prediction of dpa inaccurate. Experimentally the stored energy in the material, which quantifies the extent of irradiation damage, has been determined using differential scanning calorimetry [65–67]. The extent of damage in the configurations from MD simulation could be correlated with the stored potential energy of the system after cascade cooling. This stored energy includes the energy due to the trapped point defects, number of clusters and the displacement of the atoms in the material. In the present work, the potential energy of the pristine and irradiated GB configurations was found to be of the same order and their difference negligible and lying within scatter, as seen in Fig. 11a and listed in Table in supplementary section. Thus it is difficult to comment on the extent of damage based on the changes in potential energy before and after collision cascade. Further the average displacement of atoms after cooling of cascade were similar for all configurations and within the scatter as seen in Table A2 of Appendix.

The tensile simulations of irradiated GB configurations showed nucleation of dislocations from radiation induced defects. Dislocations loops of type $\frac{a}{2}\langle 1\,1\,1\rangle$ nucleated from faults on {110}. Similar type of dislocation loop nucleation from clusters was

observed by Wirth et al. [34] and Marian et al. [35]. The difference in UTS between pristine and irradiated GB configurations can be related to the trapped radiation induced defects and their clusters. Kang et al. used MD simulation to study the effect of uniaxial stress on interstitial defects in α-Fe. They concluded that the $\langle 1\,1\,0 \rangle$ and $\langle 1\,1\,1 \rangle$ oriented defects had reduced formation energy as a function of strain [60]. Experimental irradiation results [68,69] have shown that irradiation hardening of the material is due to the increase in defect density (both point as well as line defects). In the present MD simulations, the initial configuration had only GB as defects. After collision cascade simulations, the irradiation induced defects (vacancies and interstitials) increased. Whereas configurations with LAGB, HAGB and Σ 11 showed no change in UTS after cascade collision, the configuration with Σ 3 GBs showed a decrease in UTS (Fig. 11b) highlighting the special character of Σ 3 GB. The error bars correspond to the six repetition of simulation. GBs with $[\bar{1}\,1\,0]$ tilt axis showed better sink strength and good irradiation resistance while maintaining their mechanical strength.

5. Conclusion

This study brought out the interaction of collision cascade induced defects with different types of grain boundaries and the
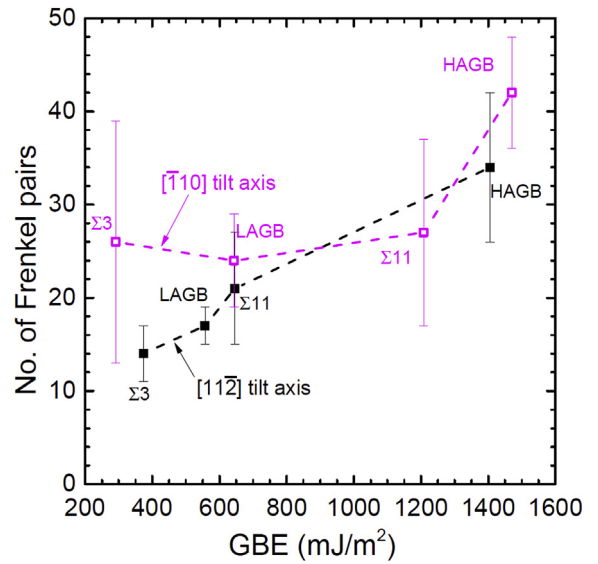
Fig. 9. Variation of number of Frenkel pairs as a function of GBE. The error bars were obtained from the six separate simulations for each condition as described in section 2.3 and listed in Table A1 in Appendix.
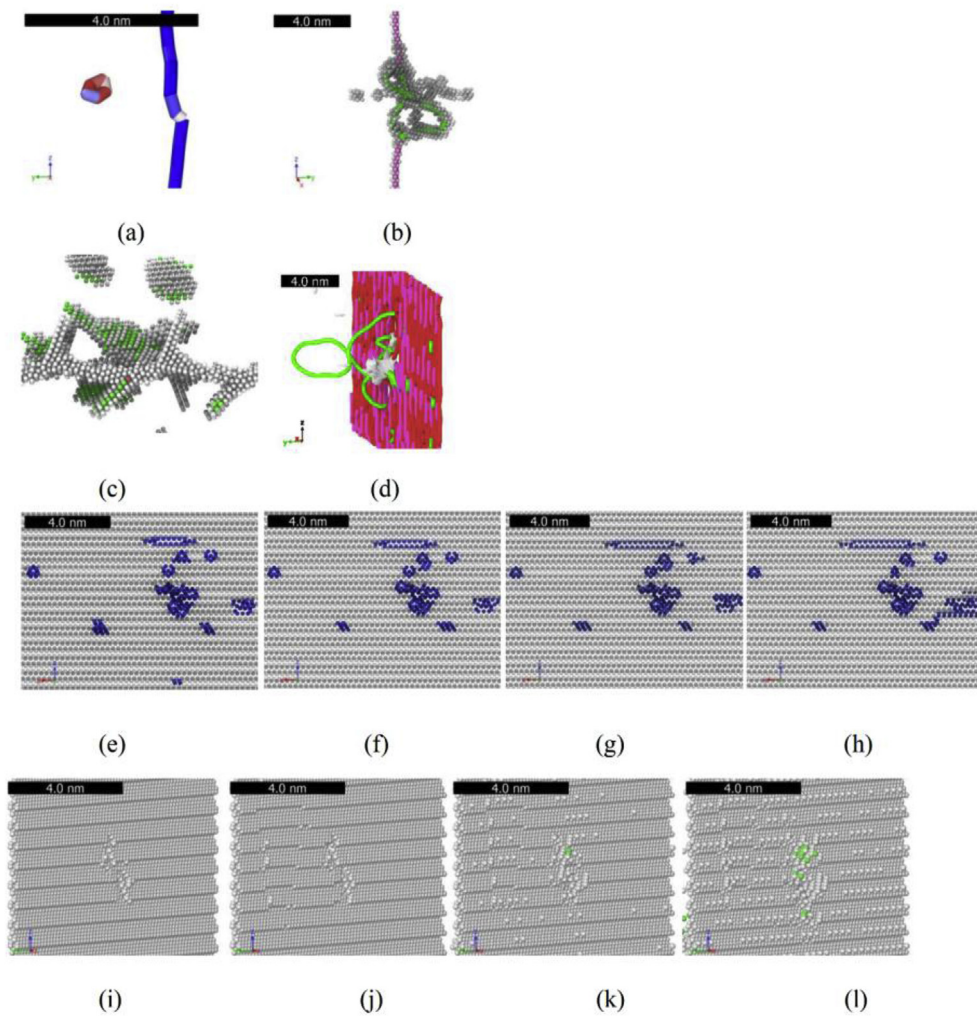
Fig. 8. Defects observed during tensile loading simulations. (a) DXA of LAGB with $[11\bar{2}]$ tilt axis shows nucleation of dislocation loop. Blue lines represent edge type dislocation, red lines represent screw type dislocations and white lines represent mixed type dislocations. (b) Interaction of dislocation loop with dislocation in the LAGB with $[\bar{1}10]$ tilt axis. Pink lines represent sessile dislocations and green lines represent glissile dislocations and white colored atoms represent non-bcc atoms. (c) Nucleation of dislocation in HAGB with $[11\bar{2}]$ tilt axis. Green colored atoms represent fcc type atoms. (d) Interaction of dislocation loops. Red lines represent dislocation type other than sessile and glissile. (e, f, g, h) Expansion of fault in Σ 3 GBs with $[11\bar{2}]$ tilt axis. Blue colored atoms represent atoms around the fault in the GB. (i, j, k, l) Failure of Σ 11 GB with $[11\bar{2}]$ tilt axis. (For interpretation of the references to color in this figure legend, the reader is referred to the Web version of this article.)
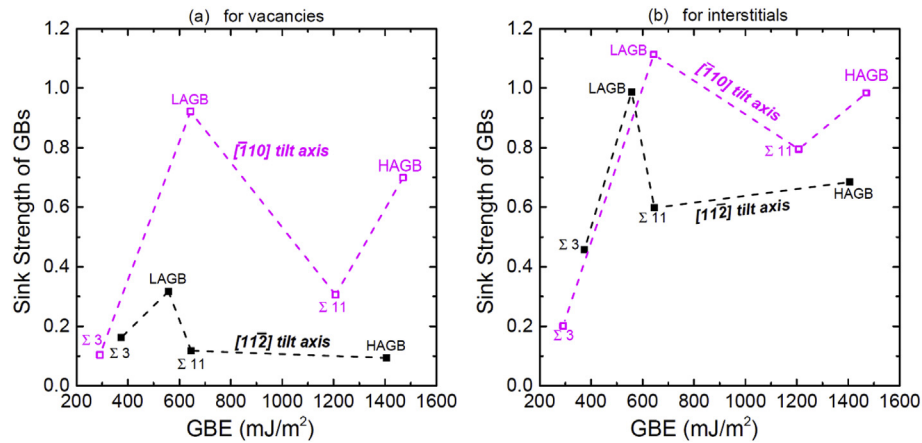
Fig. 10. Sink strength of the GBs as a function of GBE for (a) vacancies and (b) interstitials.
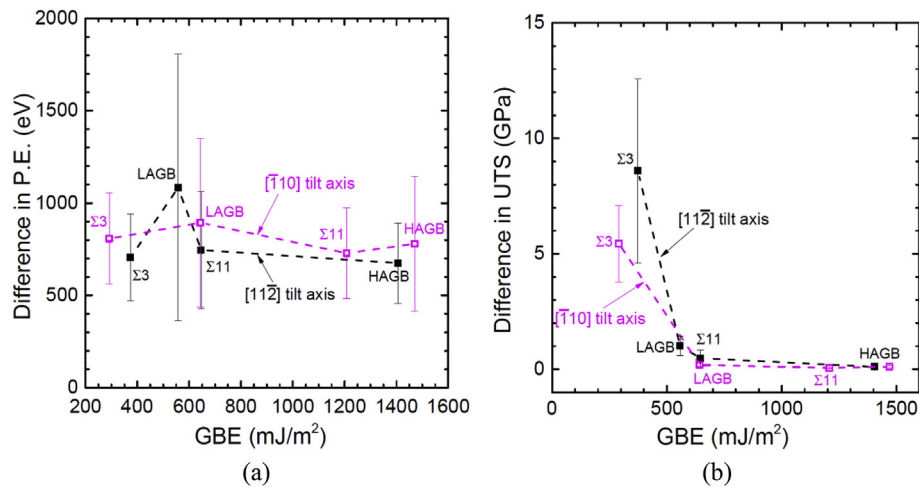

Fig. 11. Difference before and after irradiation in (a) potential energy and (b) UTS plotted vs. grain boundary energy. The error bars were obtained from the six separate simulations for each condition as described in section 2.3 and listed in Table A3 and A4 in Appendix.

subsequent strength of the configuration. The number of Frenkel pairs remaining in the system were affected by the sink strength of the grain boundary, which in turn depended on the grain boundary energy, grain boundary structure and stress fields in the grain boundary. It was seen that Σ 3 GB configuration had low number and HAGB high number of Frenkel pairs. It was seen that dislocations in LAGBs were good at self-healing and acted as sites for sinks for irradiation induced defects while maintaining the overall strength of the configuration. The average displacement and change in potential energy before and after irradiation was similar for all grain boundary configurations. A loss in strength after collision cascade was predominantly seen in the configuration with Σ 3 GBs and was attributed to its inability to act as sinks for irradiation induced defects. Configurations with LAGB and HAGB showed the formation of kinks, dislocation loops and dislocation nodes. The property of LAGBs and dislocations to act as sinks for irradiation induced defects could help towards creating radiation resistant materials through grain boundary engineering.

Data availability statement

The raw data may be made available on request.

Appendix A. Supplementary data

Supplementary data to this article can be found online at https://doi.org/10.1016/j.jnucmat.2019.06.021.

Appendix

Six simulations were carried out for each grain boundary configuration − at two temperatures 0 K and 5 K and with PKA in three different orientations to the grain boundary normal, 0° perpendicular to grain boundary, 2° (in positive x direction) and −2° (in negative x direction). The number of Frenkel pairs, average displacement of atoms, UTS and PE for each of these simulations are listed in Table below.

Table A1
Number of Frenkel pairs

Temp(K)	PKA tilt (°)	Tilt angle of GBs with $[1\,1\,\bar{2}]$ tilt axis				Tilt angle of GBs with $[\bar{1}\,1\,0]$ tilt axis			
		4.92°	32.51°	62.96°	180°	4.91°	31.59°	70.53°	129.52°
0	0	18	27	23	11	25	52	34	31
0	2	18	48	20	14	22	43	38	42
0	−2	20	29	14	12	21	35	41	22
5	0	17	32	22	14	24	44	18	19
5	2	14	31	30	17	17	37	13	16
5	−2	17	34	16	18	32	39	14	32
Mean ± stdev		17 ± 2	34 ± 7	21 ± 5	14 ± 3	24 ± 5	42 ± 6	26 ± 12	27 ± 9

Table A2
Average displacement of atoms (pm)

Temp(K)	PKA tilt (°)	Tilt angle of GBs with $[1\,1\,\bar{2}]$ tilt axis				Tilt angle of GBs with $[\bar{1}\,1\,0]$ tilt axis			
		4.92°	32.51°	62.96°	180°	4.91°	31.59°	70.53°	129.52°
0	0	1.49	2.40	2.34	1.74	1.82	1.82	1.75	1.86
0	2	1.48	2.40	2.50	1.93	1.86	1.86	1.70	1.95
0	−2	1.51	2.45	2.35	1.94	1.95	1.77	1.74	1.99
5	0	2.99	3.55	4.17	3.56	3.59	3.39	3.61	3.41
5	2	2.96	3.63	4.49	3.51	3.54	3.44	3.84	3.74
5	−2	3.11	3.41	4.40	3.81	3.85	3.34	3.93	3.57
Mean		2.26	2.97	3.38	2.75	2.77	2.60	2.76	2.75
± stdev		±0.84	±0.61	±1.08	±0.97	±0.98	±0.86	±1.14	±0.91

Table A3
Potential energy (P.E.) (MeV)

Temp(K)	PKA tilt (°)	Tilt angle of GBs with $[1\,1\,\bar{2}]$ tilt axis				Tilt angle of GBs with $[\bar{1}\,1\,0]$ tilt axis			
		4.92°	32.51°	62.96°	180°	4.91°	31.59°	70.53°	129.52°
0	0	−10.2964	−5.04175	−5.73734	−4.96052	−7.33588	−6.16799	−5.48784	−5.31803
0	2	−10.2963	−5.04169	−5.73731	−4.96049	−7.33584	−6.16797	−5.48779	−5.31796
0	−2	−10.2963	−5.04172	−5.73731	−4.96049	−7.33584	−6.16796	−5.48778	−5.31801
5	0	−10.295	−5.04132	−5.73673	−4.96008	−7.33503	−6.16731	−5.48734	−5.31755
5	2	−10.295	−5.04133	−5.73673	−4.96007	−7.33503	−6.16730	−5.48735	−5.31757
5	−2	−10.295	−5.04132	−5.73675	−4.96006	−7.33501	−6.16731	−5.48736	−5.31754
Initial value		−10.297	−5.0422	−5.73777	−4.96099	−7.33633	−6.16842	−5.48838	−5.3185

Table A4
UTS (GPa)

Temp(K)	PKA tilt (°)	Tilt angle of GBs with $[1\,1\,\bar{2}]$ tilt axis				Tilt angle of GBs with $[\bar{1}\,1\,0]$ tilt axis			
		4.92°	32.51°	62.96°	180°	4.91°	31.59°	70.53°	129.52°
0	0	25.73	16.4	15.6	27.49	20.56	18.97	27.6	14.21
0	2	24.65	16.37	15.67	27.49	20.59	18.93	27.45	14.2
0	−2	24.95	16.42	16.48	16.47	20.6	19.05	26.74	14.19
5	0	25.41	16.48	15.55	27.14	20.67	18.96	27.94	14.19
5	2	25.67	16.47	15.62	26.5	20.66	19.03	31.11	14.16
5	−2	25.17	16.49	15.59	27.43	20.75	19.02	29.78	14.16
Mean		25.3	16.4	15.8	25.42	20.6	19.0	28.4	14.2
± stdev		±0.42	±0.05	±0.36	±4.4	±0.07	±0.05	±1.66	±0.02

References

[1] B. Raj, U.K. Mudali, M. Vijayalakshmi, M.D. Mathew, A.K. Bhaduri, P. Chellapandi, S. Venugopal, C.S. Sundar, B.P.C. Rao, B. Venkataraman, Development of stainless steels in nuclear industry: with emphasis on sodium cooled fast spectrum reactors: history, technology and foresight, Century Stainl. Steels. 794 (2013) 3—25, https://doi.org/10.4028/www.scientific.net/AMR.794.3.

[2] S.J. Zinkle, Advanced materials for fusion technology, Fusion Eng. Des. 74 (2005) 31—40, https://doi.org/10.1016/j.fusengdes.2005.08.008.

[3] J.C. van Duysen, G. Meric de Bellefon, 60th Anniversary of electricity production from light water reactors: historical review of the contribution of materials science to the safety of the pressure vessel, J. Nucl. Mater. 484 (2017) 209—227, https://doi.org/10.1016/j.jnucmat.2016.11.013.

[4] S.J. Zinkle, G.S. Was, Materials challenges in nuclear energy, Acta Mater. 61 (2013) 735—758, https://doi.org/10.1016/j.actamat.2012.11.004.

[5] T. Jayakumar, M.D. Mathew, K. Laha, High temperature materials for nuclear fast fission and fusion reactors and advanced fossil power plants, Procedia Eng 55 (2013) 259—270, https://doi.org/10.1016/j.proeng.2013.03.252.

[6] J. Byggmästar, F. Granberg, K. Nordlund, Molecular dynamics simulations of thermally activated edge dislocation unpinning from voids in α-Fe, Phys. Rev. Mater. 1 (2017), https://doi.org/10.1103/PhysRevMaterials.1.053603, 053603.

[7] R. Alexander, M.C. Marinica, L. Proville, F. Willaime, K. Arakawa, M.R. Gilbert, S.L. Dudarev, Ab initio scaling laws for the formation energy of nanosized interstitial defect clusters in iron, tungsten, and vanadium, Phys. Rev. B 94 (2016) 1—15, https://doi.org/10.1103/PhysRevB.94.024103.

[8] G.J. Galloway, G.J. Ackland, Molecular dynamics and object kinetic Monte Carlo study of radiation-induced motion of voids and He bubbles in bcc iron, Phys. Rev. B Condens. Matter 87 (2013) 10—15, https://doi.org/10.1103/PhysRevB.87.104106.

[9] P. Brommer, L.K. Béland, J.F. Joly, N. Mousseau, Understanding long-time vacancy aggregation in iron: a kinetic activation-relaxation technique study,

Phys. Rev. B Condens. Matter 90 (2014) 1—9, https://doi.org/10.1103/PhysRevB.90.134109.

[10] V. Kuksenko, C. Pareige, C. Genevois, F. Cuvilly, M. Roussel, P. Pareige, Effect of neutron-irradiation on the microstructure of a Fe-12at.%Cr alloy, J. Nucl. Mater. 415 (2011) 61—66, https://doi.org/10.1016/j.jnucmat.2011.05.042.

[11] V. Kuksenko, C. Pareige, P. Pareige, Intra granular precipitation and grain boundary segregation under neutron irradiation in a low purity Fe-Cr based alloy, J. Nucl. Mater. 425 (2012) 125—129, https://doi.org/10.1016/j.jnucmat.2011.10.031.

[12] V. Kuksenko, C. Pareige, P. Pareige, Cr precipitation in neutron irradiated industrial purity Fe-Cr model alloys, J. Nucl. Mater. 432 (2013) 160—165, https://doi.org/10.1016/j.jnucmat.2012.07.021.

[13] V. Kuksenko, C. Pareige, C. Genevois, P. Pareige, Characterisation of Cr, Si and P distribution at dislocations and grain-boundaries in neutron irradiated Fe-Cr model alloys of low purity, J. Nucl. Mater. 434 (2013) 49—55, https://doi.org/10.1016/j.jnucmat.2012.11.027.

[14] D. Kaoumi, J. Adamson, M. Kirk, Microstructure evolution of two model ferritic/martensitic steels under in situ ion irradiation at low doses (0-2 dpa), J. Nucl. Mater. 445 (2014) 12—19, https://doi.org/10.1016/j.jnucmat.2013.10.047.

[15] Z. Jiao, G.S. Was, Novel features of radiation-induced segregation and radiation-induced precipitation in austenitic stainless steels, Acta Mater. 59 (2011) 1220—1238, https://doi.org/10.1016/j.actamat.2010.10.055.

[16] Z. Jiao, G.S. Was, Segregation behavior in proton- and heavy-ion-irradiated ferritic-martensitic alloys, Acta Mater. 59 (2011) 4467—4481, https://doi.org/10.1016/j.actamat.2011.03.070.

[17] Z. Jiao, V. Shankar, G.S. Was, Phase stability in proton and heavy ion irradiated ferritic-martensitic alloys, J. Nucl. Mater. 419 (2011) 52—62, https://doi.org/10.1016/j.jnucmat.2011.08.020.

[18] C.D. Hardie, G.R. Odette, Y. Wu, S. Akhmadaliev, S.G. Roberts, Mechanical properties and plasticity size effect of Fe-6%Cr irradiated by Fe ions and by neutrons, J. Nucl. Mater. 482 (2016) 236—247, https://doi.org/10.1016/j.jnucmat.2016.10.028.

[19] C.D. Hardie, S.G. Roberts, Nanoindentation of model Fe-Cr alloys with self-ion irradiation, J. Nucl. Mater. 433 (2013) 174—179, https://doi.org/10.1016/j.jnucmat.2012.09.003.

[20] J.P. Wharry, Z. Jiao, V. Shankar, J.T. Busby, G.S. Was, Radiation-induced segregation and phase stability in ferritic-martensitic alloy T 91, J. Nucl. Mater. 417 (2011) 140—144, https://doi.org/10.1016/j.jnucmat.2010.12.052.

[21] J.P. Wharry, G.S. Was, The mechanism of radiation-induced segregation in ferritic-martensitic alloys, Acta Mater. 65 (2014) 42—55, https://doi.org/10.1016/j.actamat.2013.09.049.

[22] J.P. Wharry, M.J. Swenson, K.H. Yano, A review of the irradiation evolution of dispersed oxide nanoparticles in the b.c.c. Fe-Cr system: current understanding and future directions, J. Nucl. Mater. 486 (2017) 11—20, https://doi.org/10.1016/j.jnucmat.2017.01.009.

[23] M.B. Toloczko, F.A. Garner, V.N. Voyevodin, V.V. Bryk, O.V. Borodin, V.V. Mel'Nychenko, A.S. Kalchenko, Ion-induced swelling of ODS ferritic alloy MA957 tubing to 500 dpa, J. Nucl. Mater. 453 (2014) 323—333, https://doi.org/10.1016/j.jnucmat.2014.06.011.

[24] A. Etienne, B. Radiguet, N.J. Cunningham, G.R. Odette, R. Valiev, P. Pareige, Comparison of radiation-induced segregation in ultrafine-grained and conventional 316 austenitic stainless steels, Ultramicroscopy 111 (2011) 659—663, https://doi.org/10.1016/j.ultramic.2010.12.026.

[25] A. Etienne, B. Radiguet, P. Pareige, Understanding silicon-rich phase precipitation under irradiation in austenitic stainless steels, J. Nucl. Mater. 406 (2010) 251—256, https://doi.org/10.1016/j.jnucmat.2010.08.045.

[26] C. Björkas, K. Nordlund, M.J. Caturla, Influence of the picosecond defect distribution on damage accumulation in irradiated α-Fe, Phys. Rev. B Condens. Matter 85 (2012) 1—8, https://doi.org/10.1103/PhysRevB.85.024105.

[27] M.W. Guinan, J.H. Kinney, Molecular dynamic calculations of energetic displacement cascades, J. Nucl. Mater. 104 (1981) 1319—1323, https://doi.org/10.1016/0022-3115(82)90782-6.

[28] C.G. Zhang, Y.G. Li, W.H. Zhou, L. Hu, Z. Zeng, Anti-radiation mechanisms in nanoporous gold studied via molecular dynamics simulations, J. Nucl. Mater. 466 (2015) 328—333, https://doi.org/10.1016/j.jnucmat.2015.08.003.

[29] C.G.G. Zhang, W.H.H. Zhou, Y.G.G. Li, Z. Zeng, X. Ju, Primary radiation damage near grain boundary in bcc tungsten by molecular dynamics simulations, J. Nucl. Mater. 458 (2015) 138—145, https://doi.org/10.1016/j.jnucmat.2014.11.135.

[30] D.J. Bacon, F. Gao, Y.N. Osetsky, The Primary damage state in fcc, bcc and hcp metals as seen in molecular dynamics simulations, J. Nucl. Mater. 276 (2000) 1—12, https://doi.org/10.1016/S0022-3115(99)00165-8.

[31] D.A. Terentyev, L. Malerba, M. Hou, Dimensionality of interstitial cluster motion in bcc-Fe, Phys. Rev. B Condens. Matter 75 (2007) 1—13, https://doi.org/10.1103/PhysRevB.75.104108.

[32] P.M. Derlet, D. Nguyen-Manh, S.L. Dudarev, Multiscale modeling of crowdion and vacancy defects in body-centered-cubic transition metals, Phys. Rev. B Condens. Matter 76 (2007) 1—22, https://doi.org/10.1103/PhysRevB.76.054107.

[33] P. Olsson, T.P.C. Klaver, C. Domain, Ab initio study of solute transition-metal interactions with point defects in bcc Fe, Phys. Rev. B Condens. Matter 81 (2010) 1—12, https://doi.org/10.1103/PhysRevB.81.054102.

[34] B.D. Wirth, G.R. Odette, J. Marian, L. Ventelon, J.A. Young-Vandersall, L.A. Zepeda-Ruiz, Multiscale modeling of radiation damage in Fe-based alloys

[35] J. Marian, B.D. Wirth, R. Schäublin, G.R. Odette, J.M. Perlado, MD modeling of defects in Fe and their interactions, J. Nucl. Mater. (2003) 181—191, https://doi.org/10.1016/j.jnucmat.2003.08.037.

[36] C. Campañá, K.P. Boyle, R.E. Miller, Grain boundary motion assisted via radiation cascades in bcc Fe, Phys. Rev. B Condens. Matter 78 (2008) 1—8, https://doi.org/10.1103/PhysRevB.78.134114.

[37] A. Dunn, B. Muntifering, R. Dingreville, K. Hattar, L. Capolungo, Displacement rate and temperature equivalence in stochastic cluster dynamics simulations of irradiated pure α-Fe, J. Nucl. Mater. 480 (2016) 129—137, https://doi.org/10.1016/j.jnucmat.2016.08.018.

[38] X. Li, W. Liu, Y. Xu, C.S. Liu, Q.F. Fang, B.C. Pan, Z. Wang, Energetic and kinetic behaviors of small vacancy clusters near a symmetric Σ5(3 1 0)/[0 0 1] tilt grain boundary in bcc Fe, J. Nucl. Mater. 440 (2013) 250—256, https://doi.org/10.1016/j.jnucmat.2013.05.021.

[39] D.J. Bacon, T. Diaz de la Rubia, Molecular dynamics computer simulations of displacement cascades in metals, J. Nucl. Mater. 216 (1994) 275—290, https://doi.org/10.1016/0022-3115(94)90016-7.

[40] F.J. Pérez Pérez, R. Smith, Modelling radiation effects at grain boundaries in bcc iron, Nucl. Instrum. Methods Phys. Res. Sect. B Beam Interact. Mater. Atoms 153 (1999) 136—141, https://doi.org/10.1016/S0168-583X(99)00197-4.

[41] F.J. Pérez-Pérez, R. Smith, Structural changes at grain boundaries in bcc iron induced by atomic collisions, Nucl. Instrum. Methods Phys. Res. Sect. B Beam Interact. Mater. Atoms 164 (2000) 487—494, https://doi.org/10.1016/S0168-583X(99)01141-6.

[42] A. Behera, M.M. Ghosh, Effect of irradiation on the tensile properties of nano-sized Ti-Al alloy single crystals: a study using molecular dynamics simulations, Mater. Today Proc. 5 (2018) 20647—20651, https://doi.org/10.1016/j.matpr.2018.06.447.

[43] L. Chen, L.Q. Li, H.R. Gong, J.L. Fan, W. Li, Irradiation effect on mechanical properties of tungsten from molecular dynamic simulation, Mater. Lett. (2019), https://doi.org/10.1016/j.matlet.2019.01.043.

[44] S. Liu, L. Xie, Q. Peng, R. Li, Carbon nanotubes enhance the radiation resistance of bcc iron revealed by atomistic study, Materials (Basel) 12 (2019) 217, https://doi.org/10.3390/ma12020217.

[45] A. Hosseini, M.N. Nasrabadi, A. Esfandiarpour, Investigation of primary radiation damage near free surfaces in iron nanofoam with a model cylindrical nanovoids structure, Nucl. Instrum. Methods Phys. Res. Sect. B Beam Interact. Mater. Atoms 439 (2019) 43—50, https://doi.org/10.1016/j.nimb.2018.11.001.

[46] D. Mo, J. Cai, Y.L. Li, Y.D. Wang, Cascade collision near the grain boundary of Fe-Cr alloy by MD simulation, Mater. Sci. Forum 913 (2018) 642—649, https://doi.org/10.4028/www.scientific.net/MSF.913.642.

[47] M. Jin, P. Cao, S. Yip, M.P. Short, Radiation damage reduction by grain-boundary biased defect migration in nanocrystalline Cu, Acta Mater. 155 (2018) 410—417, https://doi.org/10.1016/j.actamat.2018.05.071.

[48] L. Wu, W. Yu, S. Hu, S. Shen, Radiation response of nanotwinned Cu under multiple-collision cascades, J. Nucl. Mater. 505 (2018) 183—192, https://doi.org/10.1016/j.jnucmat.2018.04.020.

[49] M. Jin, P. Cao, M.P. Short, Mechanisms of grain boundary migration and growth in nanocrystalline metals under irradiation, Scripta Mater. 163 (2019) 66—70, https://doi.org/10.1016/j.scriptamat.2018.12.038.

[50] D. Singh, A. Parashar, A. Kedharnath, R. Kapoor, A. Sarkar, Effect of symmetrical and asymmetrical tilt grain boundaries on the tensile deformation of zirconium bicrystals, J. Mater. Sci. 54 (2019) 3082—3095.

[51] S. Plimpton, Fast Parallel algorithms for short-range molecular dynamics, J. Comput. Phys. 117 (1995) 1—19, https://doi.org/10.1006/jcph.1995.1039.

[52] M.I. Mendelev, S. Han, D.J. Srolovitz, G.J. Ackland, D.Y. Sun, M. Asta, Development of new interatomic potentials appropriate for crystalline and liquid iron, Philos. Mag. A 83 (2003) 3977—3994, https://doi.org/10.1080/14786430310001613264.

[53] A. Stukowski, Visualization and analysis of atomistic simulation data with OVITO—the Open Visualization Tool, Model. Simul. Mater. Sci. Eng. 18 (2010), https://doi.org/10.1088/0965-0393/18/1/015012, 015012.

[54] A. Kedharnath, A.S. Panwar, R. Kapoor, Molecular dynamics simulation of the interaction of a nano-scale crack with grain boundaries in α-Fe, Comput. Mater. Sci. 137 (2017) 85—99, https://doi.org/10.1016/j.commatsci.2017.05.026.

[55] M.A. Tschopp, K.N. Solanki, F. Gao, X. Sun, M.A. Khaleel, M.F. Horstemeyer, Probing grain boundary sink strength at the nanoscale: energetics and length scales of vacancy and interstitial absorption by grain boundaries in α-Fe, Phys. Rev. B Condens. Matter 85 (2012) 1—21, https://doi.org/10.1103/PhysRevB.85.064108.

[56] A. Arjhangmehr, S.A.H. Feghhi, Irradiation deformation near different atomic grain boundaries in α-Zr: an investigation of thermodynamics and kinetics of point defects, Sci. Rep. 6 (2016), https://doi.org/10.1038/srep23333.

[57] C.H. Rycroft, VORO++: a three-dimensional Voronoi cell library in C++, Chaos 19 (2009) https://doi.org/10.1063/1.3215722.

[58] A. Stukowski, V. V Bulatov, A. Arsenlis, Automated identification and indexing of dislocations in crystal interfaces, Model. Sci. Eng. 20 (2012), https://doi.org/10.1088/0965-0393/20/8/085007, 085007.

[59] A. Stukowski, K. Albe, Extracting dislocations and non-dislocation crystal defects from atomistic simulation data, Model. Simul. Mater. Sci. Eng. 18 (2010), https://doi.org/10.1088/0965-0393/18/8/085001, 085001.

[60] C. Kang, Q. Wang, L. Shao, Kinetics of interstitial defects in α-Fe: the effect from uniaxial stress, J. Nucl. Mater. 485 (2017) 159–168, https://doi.org/10.1016/j.jnucmat.2016.12.015.

[61] A. Esfandiarpour, S.A.H. Feghhi, A.A. Shokri, Effects of atomic grain boundary structures on primary radiation damage in α-Fe, Nucl. Instrum. Methods Phys. Res. Sect. B Beam Interact. Mater. Atoms 362 (2015) 1–8, https://doi.org/10.1016/j.nimb.2015.08.074.

[62] M.C. Marinica, F. Willaime, N. Mousseau, Energy landscape of small clusters of self-interstitial dumbbells in iron, Phys. Rev. B Condens. Matter 83 (2011) 1–14, https://doi.org/10.1103/PhysRevB.83.094119.

[63] H. Xu, R.E. Stoller, Y.N. Osetsky, D. Terentyev, Solving the puzzle of 100 interstitial loop formation in bcc iron, Phys. Rev. Lett. 110 (2013) 1–5, https://doi.org/10.1103/PhysRevLett.110.265503.

[64] G.S. Was, Fundamentals of Radiation Materials Science, Springer, Berlin, Heidelberg, 2007, https://doi.org/10.1007/978-3-540-49472-0.

[65] P.C. Minshall, A.J. Wickham, The description of Wigner energy and its release from Windscale Pile graphite for application to waste packaging and disposal, in: Proc. IAEA Tech. Comm. Meet. Manchester, UK, 1999.

[66] R.M. Guppy, J. McCarthy, S.J. Wisbey, Technical assessment of the significance of Wigner energy for disposal of graphite wastes from the Windscale Piles, in: IAEA Tech. Comm. Meet. Held Manchester, United Kingdom, 1999, pp. 18–20.

[67] T.C. Ehlert, K.A. Gowda, F.G. Karioris, L. Cartz, Differential scanning calorimetry of heavy ion bombarded synthetic monazite, Radiat. Eff. 70 (1983) 173–181, https://doi.org/10.1080/00337578308219214.

[68] G.R. Odette, On the dominant mechanism of irradiation embrittlement of reactor pressure vessel steels, Scripta Metall. 17 (1983) 1183–1188, https://doi.org/10.1016/0036-9748(83)90280-6.

[69] G.R. Odette, T. Yamamoto, D. Klingensmith, On the effect of dose rate on irradiation hardening of RPV steels, Philos. Mag. A 85 (2005) 779–797, https://doi.org/10.1080/14786430412331319910.